Laser assisted phase transformation of carbon-based transition metal oxide electrode for high-performance supercapacitor application

Mingzhen Xiu[a,b,†], Jianghong Zhang[a,†], Yu Lu[a], Xun Cao[c], Kang Huang[d], Siyu Zhu[a], Bowei Zhang[d], Yu Liang[e], Chunwang Zhao[f], Junsheng Wu[d,*] Yizhong Huang[a,*]

[a] School of Materials Science and Engineering, Nanyang Technological University, 639798, Singapore

[b] Energy Research Institute, Interdisciplinary Graduate Programme, Nanyang Technological University 637141, Singapore

[c] Institute of Sustainability for Chemicals, Energy and Environment, Agency for Science, Technology and Research, 1 Pesek Road, Jurong Island, 627833, Singapore

[d] Institute of Advanced Materials and Technology, University of Science and Technology Beijing, Beijing, 100083, China

[e] School of Materials Science and Technology, Shenyang University of Chemical Technology, Shenyang, 110142, China

[f] School of Materials Science and Hydrogen Energy, Foshan University, Foshan, 52800, China

[*] Corresponding author at School of Materials Science and Engineering, Nanyang Technological University, 639798, Singapore

E-mail addresses: YZHuang@ntu.edu.sg (Y. Huang), wujs76@163.com (J. Wu)

† These authors contributed equally to this work.

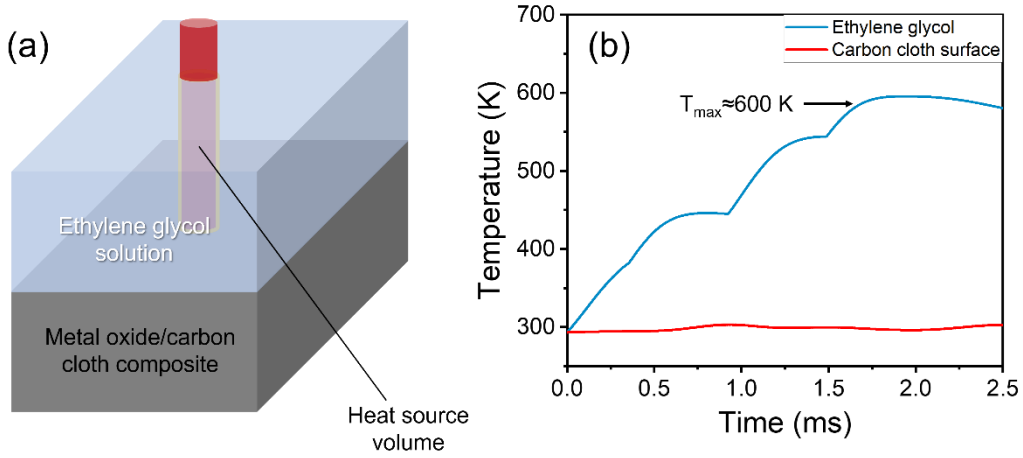

Fig. S1. (a) Illustration of laser irradiation on metal oxide/carbon composite with the presence of ethylene glycol solution. (b) Temperature dependence of laser irradiation processing time for ethylene glycol and the surface of carbon cloth substrate.

Table S1. Properties of carbon cloth

Properties	Parameters	Ref
Density	1.875 kg/m^3	[1]
Thermal conductivity	100 W/(m Ƙ) (isotropic)	[2]
Specific heat capacity	400 J/kg Ƙ	[3]

Table S2. Properties of ethylene glycol

Properties	Parameters	Ref
Density*	1322.68716 - 0.703271429T	COMSOL Multiphysics® database
Thermal conductivity (isotropic)*	-0.0376511698 + 0.00162092411T- 2.1875×10 - ^{6}T^2	

Specific heat capacity*	1071.4679 + 4.47428571T	
Absorptivity at 1064 nm	0.42	[4]

*The function interval is 273.5-373.5 K, the values at the upper and lower limit are set as the extrapolations value beyond and below the range, respectively.

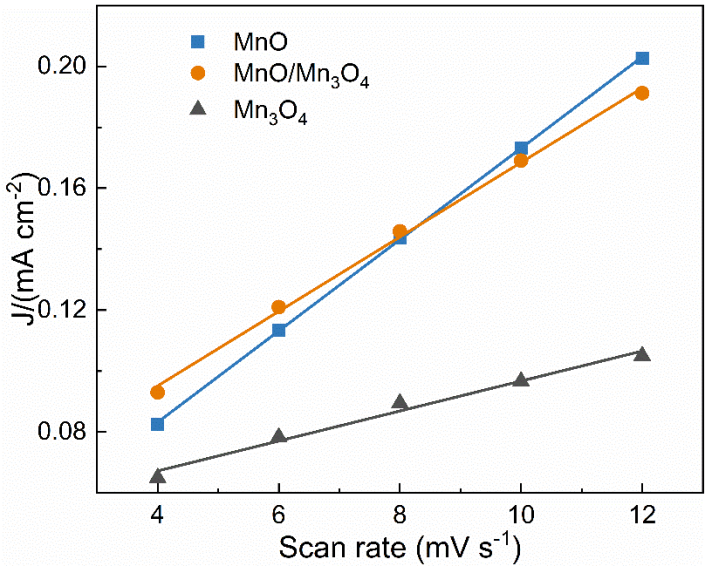

Fig. S2. ECSA of Mn_3O_4, MnO/Mn_3O_4, MnO electrodes.

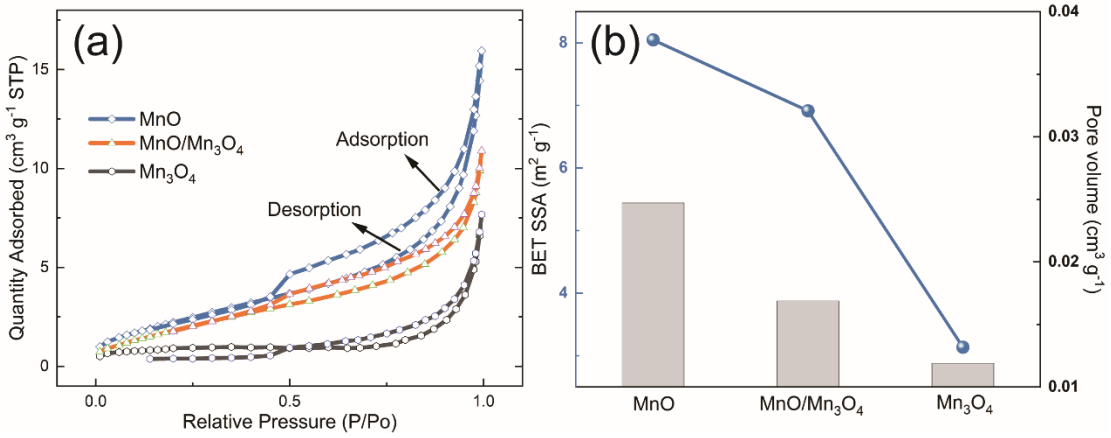

Fig. S3. (a) Nitrogen adsorption/desorption isotherms of MnO, MnO/Mn_3O_4, and Mn_3O_4/carbon cloth electrode. (b) BET specific surface area and pore volume of MnO,

MnO/Mn_3O_4, and Mn_3O_4/carbon cloth electrode.

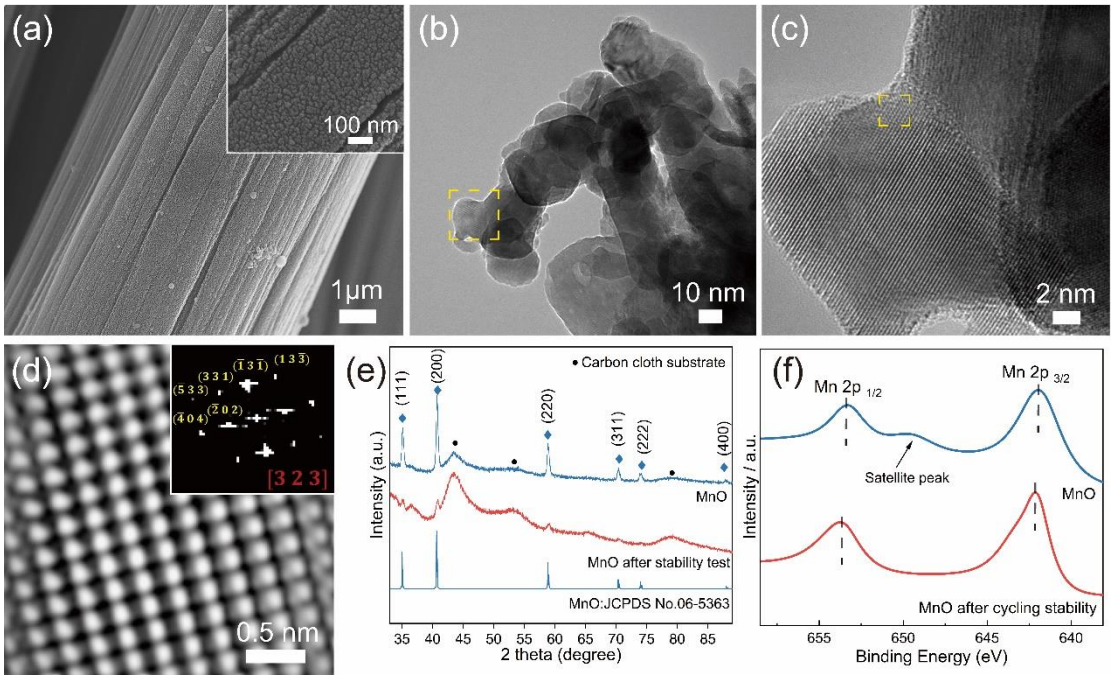

Fig. S4. Morphological and crystal structure characterization of MnO/carbon cloth electrode after long-term GCD stability test in 1 M Na_2SO_4 electrolyte. (a) FESEM image of MnO/carbon cloth electrode, (b) and (c) Low magnification TEM images of MnO nanoparticles, (d) HR TEM image of the yellow box in (c), and corresponding FFT pattern, (e) and (f) XRD and XPS (Mn 2p) analysis of MnO/carbon cloth electrode before and after the stability test are compared.

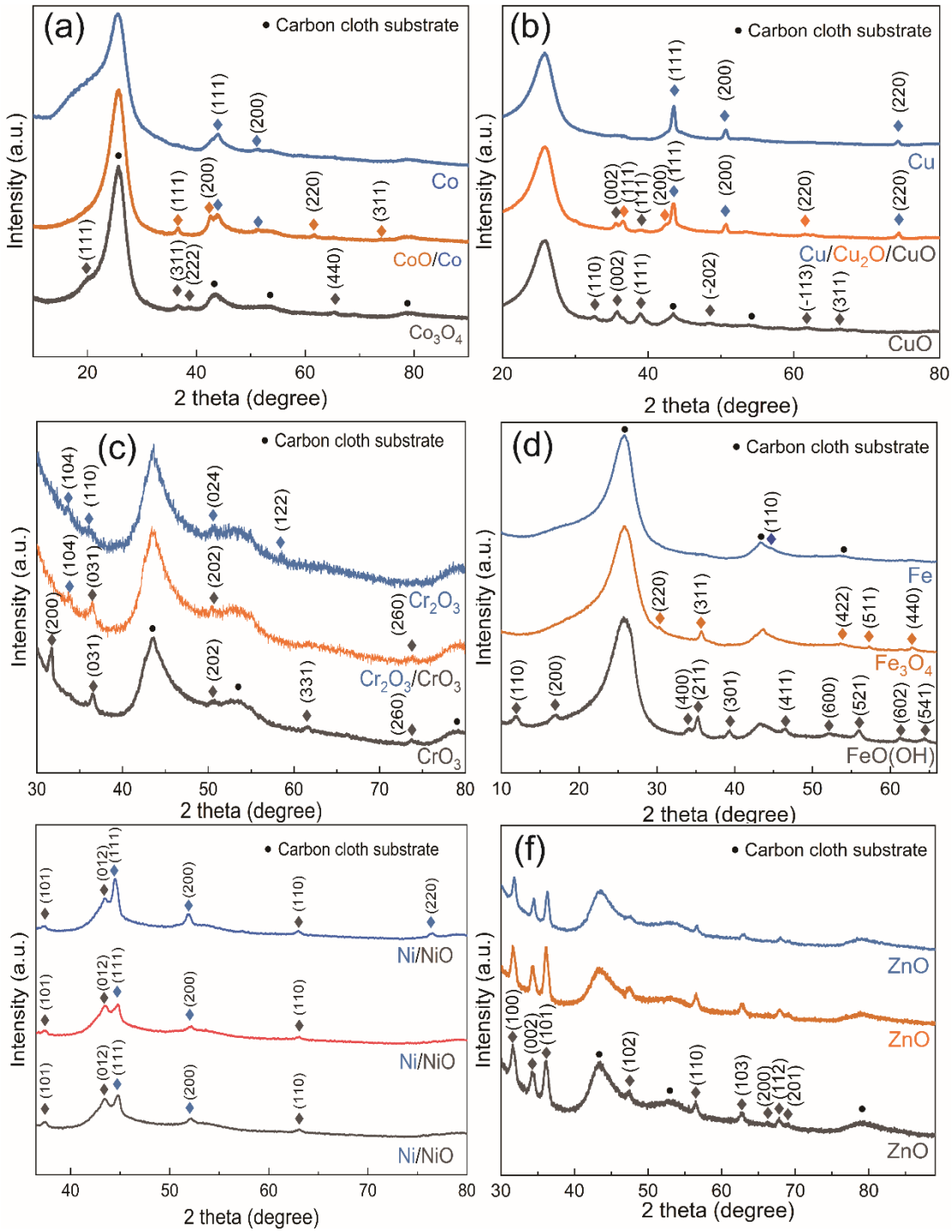

Fig. S5. XRD patterns of different LPDD synthesized transitional metals (Co, Cu, Cr, Fe, Ni, and Zn) oxides on carbon cloth substrate, after laser irradiation phase transformation without ethylene glycol, and with ethylene glycol.

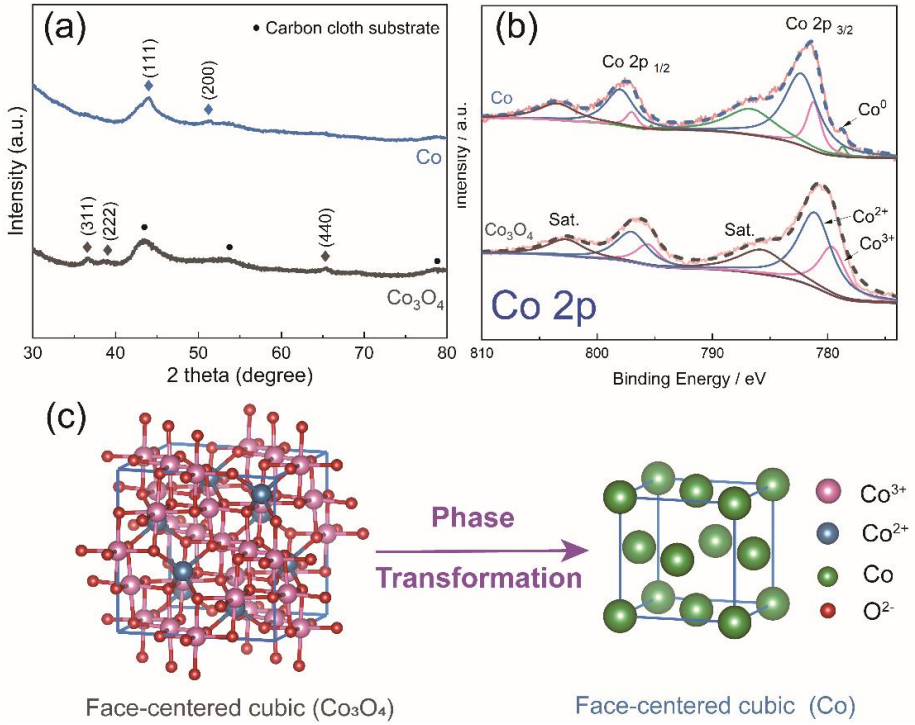

Fig. S6. (a) XRD and (b) XPS analysis of LPDD pre-synthesized Co_3O_4 and laser irradiation phase transformed Co/carbon cloth composites, (c) crystal structure models of Co_3O_4 and Co.

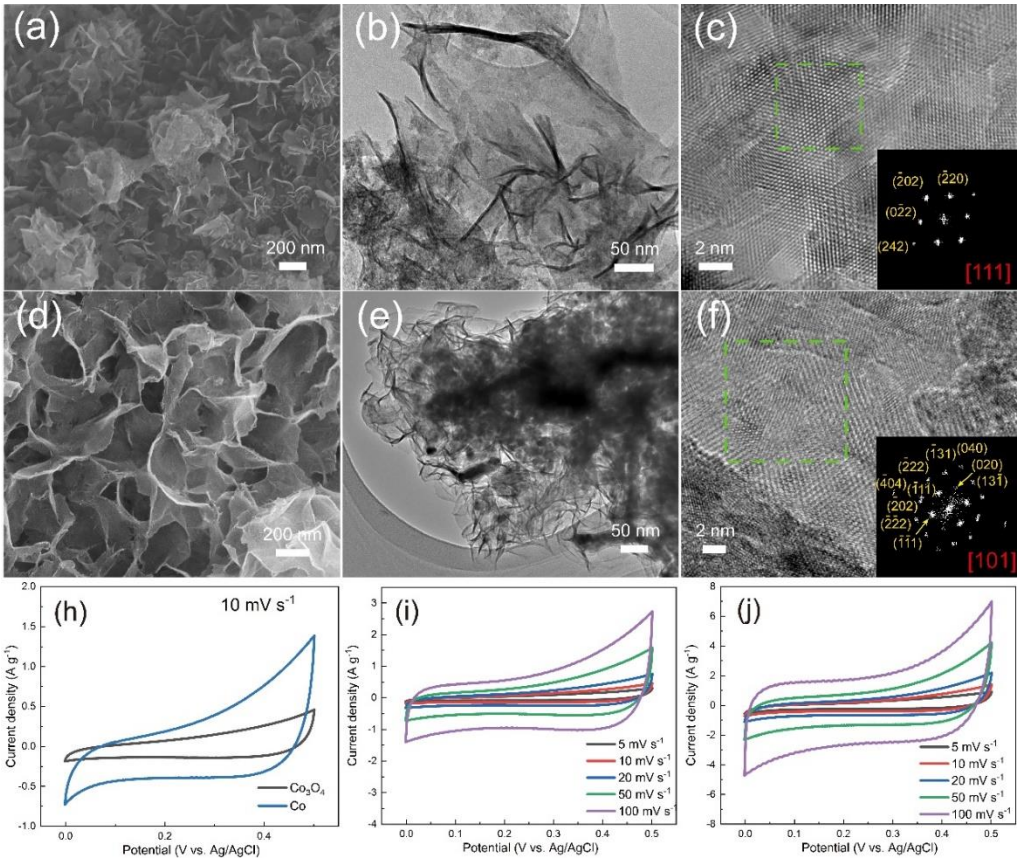

Fig. S7. (a) SEM, and (b) TEM images of LPDD synthesized Co_3O_4, (c) HR TEM image and

its corresponding FFT pattern of Co_3O_4 nanosheet; (d) SEM, and (e) TEM images of laser irradiation phase transformed Co, (c) HR TEM image and its corresponding FFT pattern of Co nanosheet; (h) CV curves of Co_3O_4 and Co/carbon cloth electrodes at a scan rate of 10 mV s^{-1} in 1M Na_2SO_4 electrolyte, CV profiles of (i) Co_3O_4 and (j) Co/carbon cloth electrodes at different scan rates.

Fig. S6 (a) shows the XRD pattern of D pLPDre-synthesized Co_3O_4 and phase-transformed Co. The pre-synthesized FCC Co_3O_4 (JCPDS 73-2750) after phase transformation via laser irradiation shows the peaks at 44.0° and 51.4°, corresponding to (1 1 1) and (2 0 0) planes of FCC Co crystal (JCPDS 71-4238). In contrast, the CoO/Co mixture was formed during phase transformation without ethylene glycol, the XRD analysis comparison between Co_3O_4, CoO/Co, and Co/carbon cloth electrodes is displayed in Fig. S5 (a). Furthermore, the XPS analysis confirms the formation of Co^0 after phase transformation. Fig. S6 (b) presents the HR spectra for the Co 2p region of LPDD synthesized Co_3O_4 and phase-transformed Co^0. The peaks observed at 778.5 eV and 775.3 eV are attributed to Co^{0+} $2p_{3/2}$ and Co^{0+} $2p_{1/2}$ respectively, and are consistent with reported data for Co^0 in literature [5]. The high magnification SEM and low magnification TEM images of LPDD pre-synthesized nanosheet structure Co_3O_4 on carbon cloth substrate are shown in Fig. S7 (a) and (b). The HR TEM image of an ultra-thin nanosheet is presented in Fig. S7 (c) and reveals the FCC lattice structure imaged at a zone axis [1 1 1] as indexed from the FFT pattern. In contrast, the morphology of Co^0 after phase transformation remains unchanged as demonstrated by the low magnification SEM and TEM images in Fig. S7 (d) and (e).

Additionally, the HR TEM image of one piece of nanosheet Co^0 was taken at a zone axis [1 0 1] indexed from the FFT pattern (inset). The CVs comparison for Co_3O_4 and Co/carbon cloth electrodes were performed and shown in Fig. S7 (g-i).

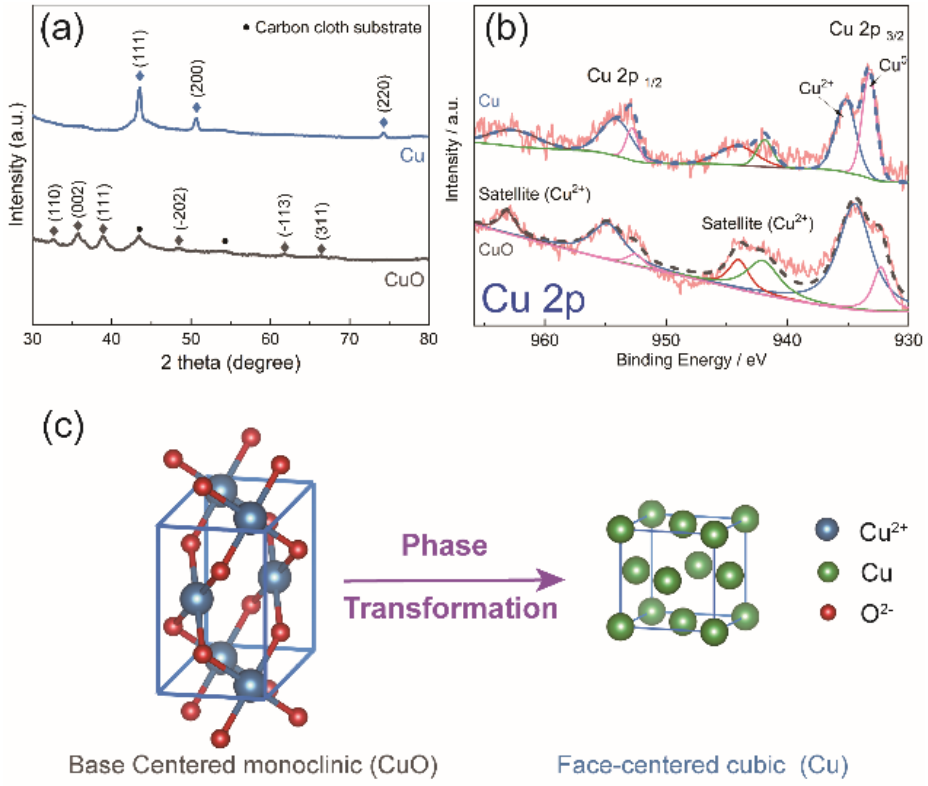

Fig. S8. (a) XRD and (b) XPS analysis of LPDD pre-synthesized CuO and laser irradiation phase transformed Cu/carbon cloth composites, (c) crystal structure models of CuO and Cu.

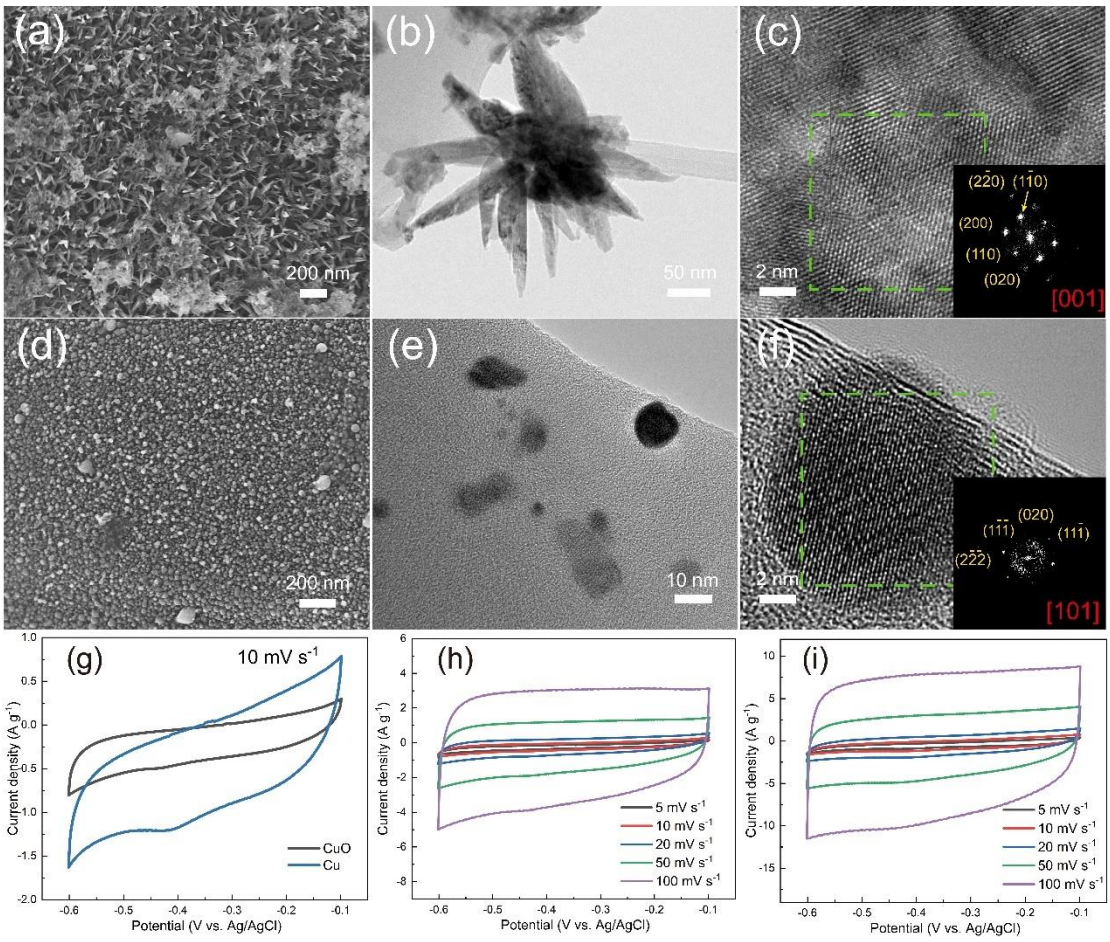

Fig. S9. (a) SEM, and (b) TEM images of LPDD synthesized CuO, (c) HR TEM image and its corresponding FFT pattern of CuO nanoneedle; (d) SEM, and (e) TEM images of laser irradiation phase transformed Cu, (c) HR TEM image and its corresponding FFT pattern of Cu nanoparticle; (h) CV curves of CuO and Cu/carbon cloth electrodes at a scan rate of 10 mV s^{-1} in 1M Na_2SO_4 electrolyte, CV profiles of (i) CuO and (j) Cu/carbon cloth electrodes at different scan rates.

The XRD analysis in Fig. S8 (a) reveals that the CuO was transformed into FCC Cu crystal after laser irradiation. The peaks observed at 43.5°, 50.7°, and 74.3°, ascribed to (1 1 1), (2 0 0), and (2 2 0) planes of FCC Cu^0 crystal (JCPDS 04-0836). However, when there was no ethylene glycol, a $Cu/Cu_2O/CuO$ mixture was formed during phase transformation. The XRD analysis of CuO, $Cu/Cu_2O/CuO$, and Cu/carbon cloth

electrodes is displayed in Fig. S5 (b). Fig. S8 (b) presents the XPS HR spectra for the Cu 2p region of CuO before and after phase transformation. Deconvolution of the Cu $2p_{3/2}$ and Cu $2p_{1/2}$ peaks shows the four peaks at 933 eV, 935 eV, 952.6 eV, and 954 eV, attributing to Cu^0 $2p_{3/2}$, Cu^{2+} $2p_{3/2}$, Cu^0 $2p_{1/2}$, and Cu^{2+} $2p_{1/2}$, respectively, which is consistent with reported data for Cu [6]. The fitting of the Cu 2p spectrum shows that the LPDD pre-synthesized CuO has a fraction of 20.4% of Cu^0 and 79.6% of Cu^{2+}, whereas the phase transformed Cu has a fraction of 50% Cu^0 and 50% of Cu^{2+}, demonstrating that the formation of Cu after laser irradiation. The crystal structure models of the phase transformation for Cu are illustrated in Fig. S8 (c). Fig. S9 (a) and (b) show the high magnification SEM and low magnification TEM images of LPDD synthesized nanoneedle CuO, which have a length of approximately 100 nm and a width of around 20 nm. The HR TEM image of one nanoneedle and its corresponding FFT pattern are displayed in Fig. S9 (c), which reveals the base centered monoclinic lattice structure imaged at a zone axis [0 0 1]. In comparison, the low magnification SEM and TEM images of spherical nanoparticles Cu after phase transformation are shown in Fig. S9 (d) and (e). The HR TEM image taken from a nanoparticle proves the FCC structure after performing the index of the reciprocal image (inset in Fig. S9 (f)). The CVs comparison for CuO and Cu/carbon cloth electrode were performed and shown in Fig. S9 (g-i).

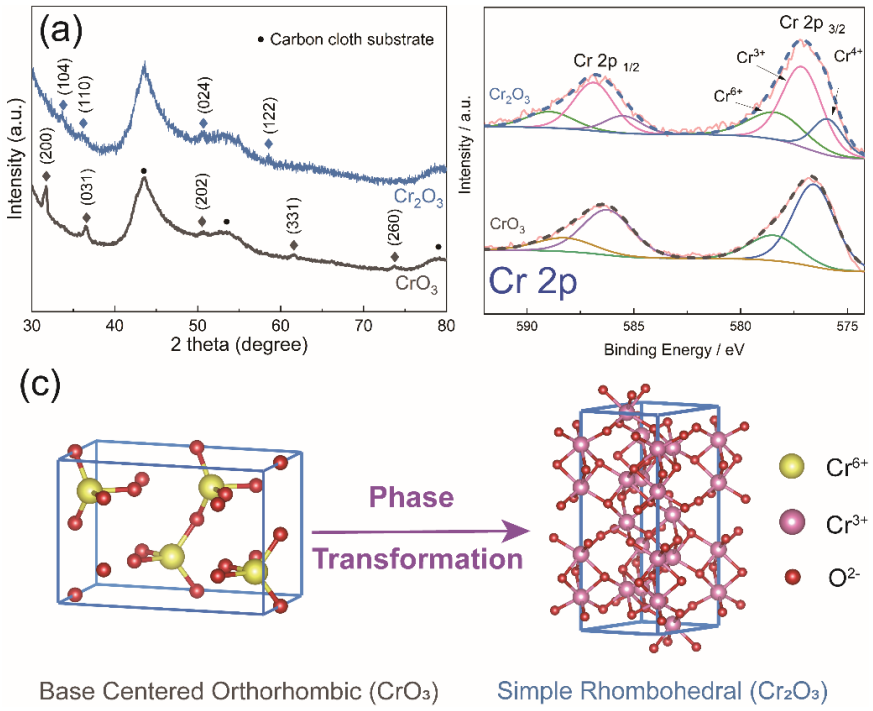

Fig. S10. (a) XRD and (b) XPS analysis of LPDD pre-synthesized CrO_3 and laser irradiation phase transformed Cr_2O_3/carbon cloth composites, (c) crystal structure models of CrO_3 and Cr_2O_3.

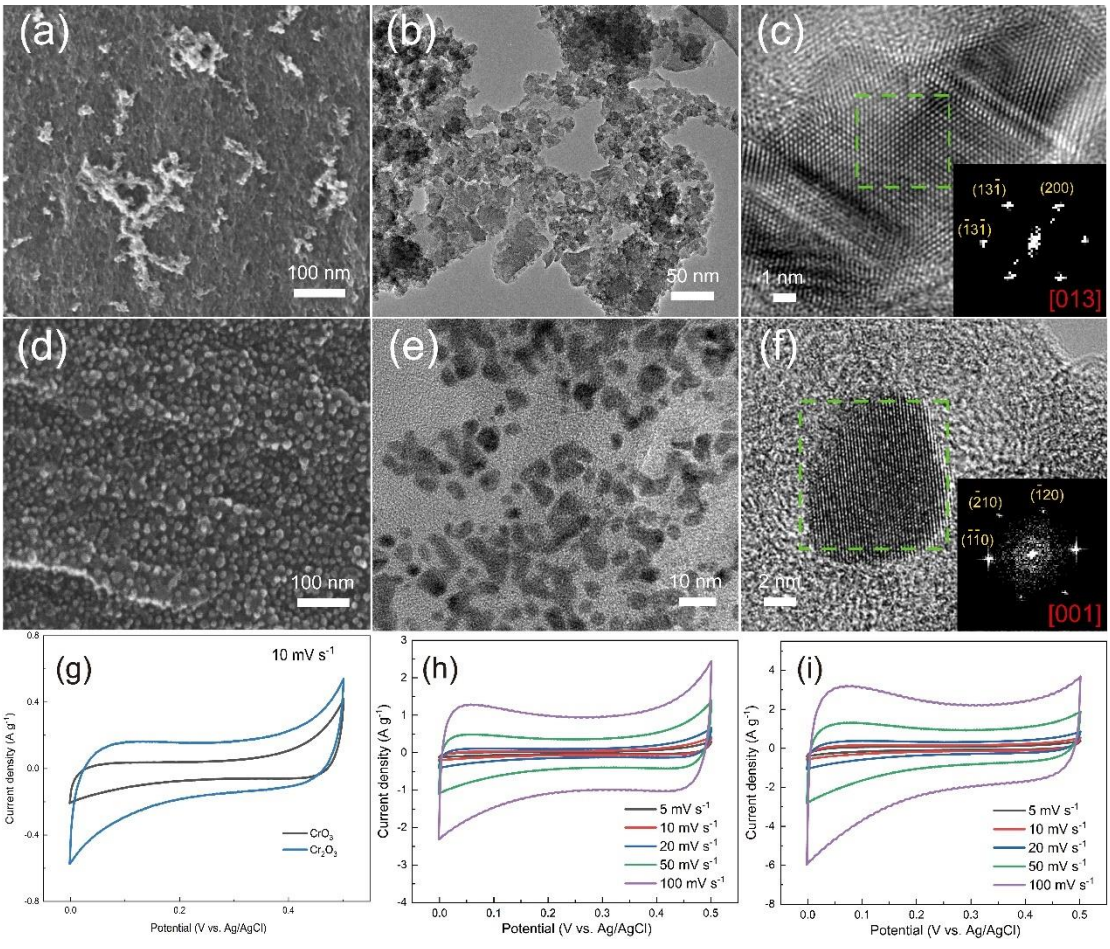

Fig. S11. (a) SEM, and (b) TEM images of LPDD synthesized CrO_3, (c) HR TEM image and its corresponding FFT pattern of CrO_3 nanoparticle; (d) SEM, and (e) TEM images of laser irradiation phase transformed Cr_2O_3, (c) HR TEM image and its corresponding FFT pattern of Cr_2O_3 nanoparticle; (h) CV curves of CrO_3 and Cr_2O_3/carbon cloth electrodes at a scan rate of 10 mV s^{-1} in 1M Na_2SO_4 electrolyte, CV profiles of (i) CrO_3 and (j) Cr_2O_3/carbon cloth electrodes at different scan rates.

Fig. S10 (a) displays the XRD patterns of pre-synthesized CrO_3 and phase transformed Cr_2O_3/carbon cloth electrode. The base centered orthorhombic CrO_3 (JCPDS 32-0285) after laser irradiation phase transformation shows the peaks at 33.8°, 36.6°, 50.4°, and 58.6°, which correspond to (1 0 4), (1 1 0), (0 2 4) and (1 2 2) planes of simple rhombohedral Cr_2O_3 crystal (JCPDS 38-1479). On the other hand, the Cr_2O_3/CrO_3 mixture was formed during phase transformation without ethylene glycol. The XRD analysis comparison between CrO_3, Cr_2O_3/CrO_3, and Cr_2O_3/carbon cloth electrodes is displayed in Fig. S5 (c). Fig. S10 (b) shows the XPS HR spectra of Cr 2p region for both samples. The Cr 2p spectrum of LPDD pre-synthesized CrO_3 shows Cr $2p_{1/2}$ and Cr $2p_{3/2}$ peaks at 576.9 eV and 586.0 eV, and the deconvolution of Cr 2p spectrum shows peaks at 576.8 eV, 578.7 eV, 585.8 eV, and 588 eV, attributing to Cr^{3+} $2p_{3/2}$, Cr^{6+} $2p_{3/2}$, Cr^{3+} $2p_{1/2}$, and Cr^{6+} $2p_{1/2}$, respectively. In contrast, the Cr 2p spectrum of Cr_2O_3 has the Cr $2p_{1/2}$ and Cr $2p_{3/2}$ peaks at a binding energy of 577.2 eV and 586.4 eV, the deconvolution of the Cr 2p spectrum of Cr_2O_3 shows peaks at 575.9 eV, 577.2 eV, 578.4 eV, 585.4 eV, 586.8 eV, and 588.9 eV attributing to $Cr^{4+}2p_{3/2}$, $Cr^{3+}2p_{3/2}$, $Cr^{6+}2p_{3/2}$, $Cr^{4+}2p_{1/2}$, $Cr^{3+}2p_{1/2}$, and $Cr^{6+}2p_{1/2}$, respectively. This confirms the formation of Cr_2O_3 after phase transformation via laser irradiation, which is consistent with

reported data in the literature [7, 8]. The crystal structure models of phase transformation for Cr are illustrated in Fig. S10 (c). The high magnification SEM and low magnification TEM images of LPDD pre-synthesized irregular shape of nanoparticles CrO_3 on carbon cloth substrate are shown in Fig. S11 (a) and (b). Fig. S11 (c) shows the HR TEM image of a single CrO_3 nanoparticle and its corresponding FFT pattern, revealing the simple orthorhombic lattice structure imaged at a zone axis [0 1 3]. In comparison, the low magnification SEM and TEM images of uniformly distributed spherical Cr_2O_3 nanoparticles on carbon cloth substrate after phase transformation via laser irradiation are shown in Fig. S11 (d) and (e). The HR TEM image of a single nanoparticle taken at a zone axis [0 0 1] indexed from the FFT pattern (inset) confirms a simple rhombohedral crystal structure. The CVs comparison for CrO_3 and Cr_2O_3/carbon cloth electrodes were performed and shown in Fig. S11 (g-i).

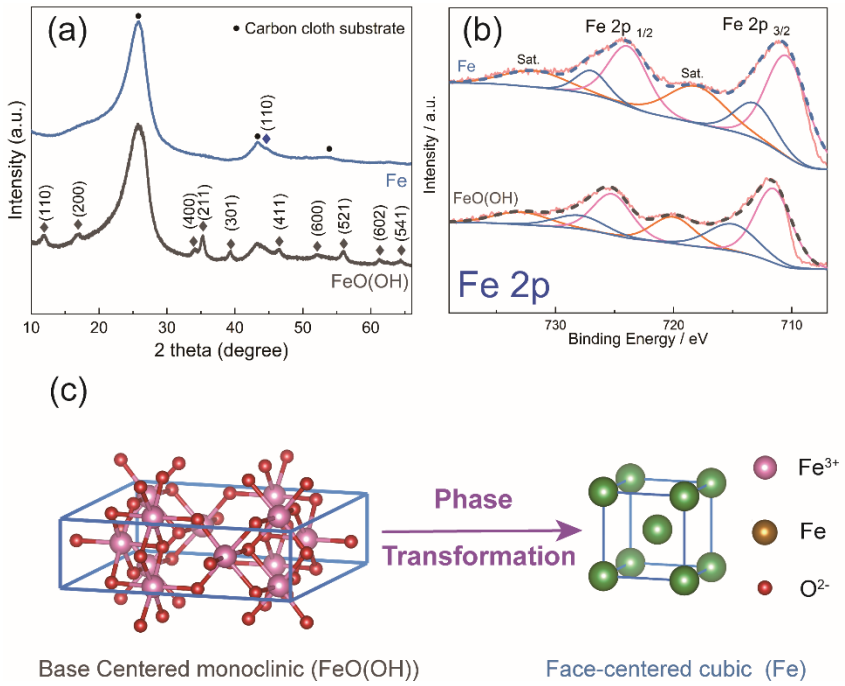

Fig. S12. (a) XRD and (b) XPS analysis of LPDD pre-synthesized FeO(OH) and laser

irradiation phase transformed Fe/carbon cloth composites, (c) crystal structure models of FeO(OH) and Fe.

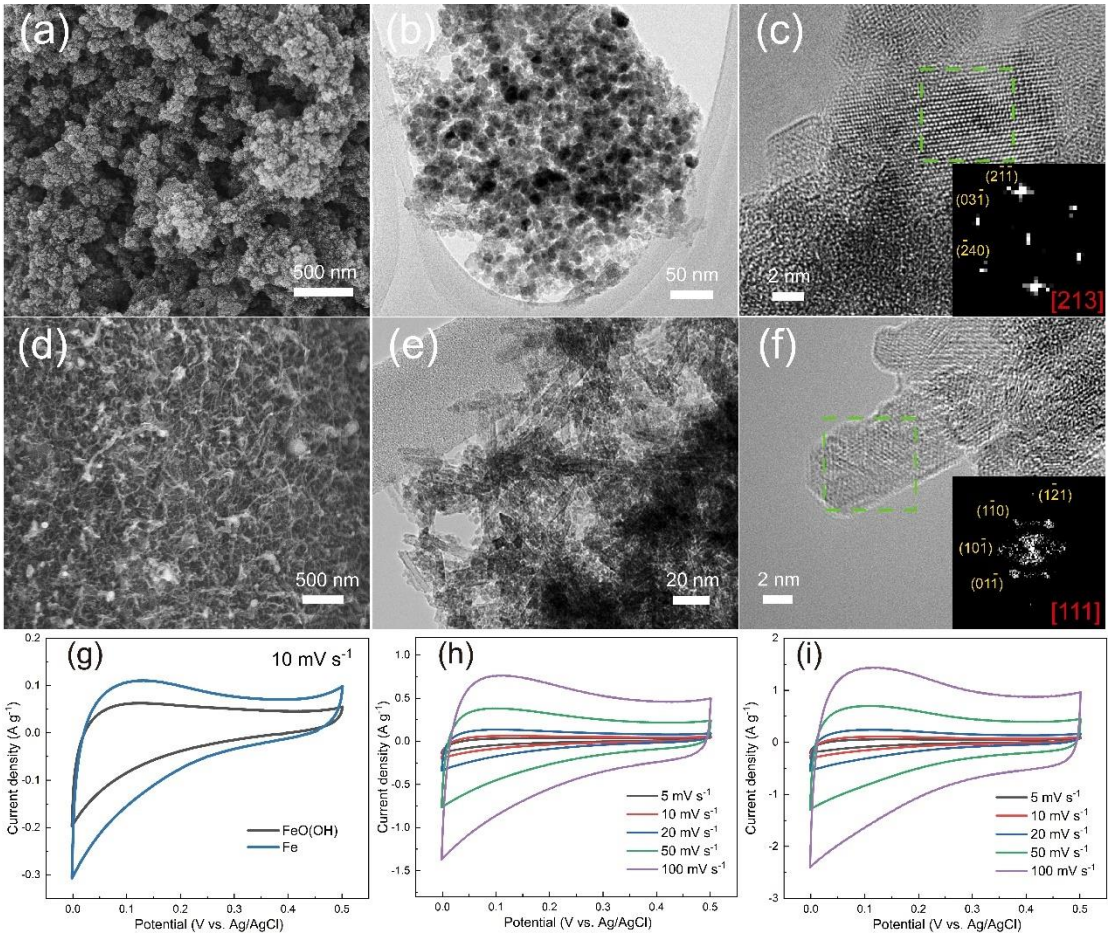

Fig. S13. (a) SEM, and (b) TEM images of LPDD synthesized FeO(OH), (c) HR TEM image and its corresponding FFT pattern of FeO(OH) nanoparticle; (d) SEM, and (e) TEM images of laser irradiation phase transformed Fe, (c) HR TEM image and its corresponding FFT pattern of Fe nanowire; (h) CV curves of FeO(OH) and Fe/carbon cloth electrodes at a scan rate of 10 mV s^{-1} in 1M Na_2SO_4 electrolyte, CV profiles of (i) FeO(OH) and (j) Fe/carbon cloth electrodes at different scan rates.

Fig. S12 (a) presents the XRD pattern of LPDD pre-synthesized FeO(OH) and phase transformed Fe on the carbon cloth substrate. The base centered monoclinic FeO(OH) (JCPDS 34-1266) after phase transformation shows the peaks at 44.7°, ascribed to the (1 1 0) plane of FCC Fe crystal (JCPDS 06-0696). In comparison, Fe_3O_4/carbon cloth

electrode was formed during phase transformation without ethylene glycol, the XRD analysis of FeO(OH), Fe_3O_4, and Fe/carbon electrodes is displayed in Fig. S5 (d). Fig. S12 (b) shows the XPS HR spectra for the Fe 2p region. The spectrum for FeO(OH) shows the peaks at 711.7 eV and 724.5 eV attributed to Fe $2p_{3/2}$ and Fe $2p_{1/2}$, whereas the Fe $2p_{3/2}$ and Fe $2p_{1/2}$ for Fe specimen show the peaks at 710.7 eV and 724 eV, which is consistent with reported data for FeO(OH) and Fe [9, 10]. The binding energies of Fe $2p_{3/2}$ and Fe $2p_{1/2}$ shift to the lower side, demonstrating the phase transformation of Fe via laser irradiation. The crystal structure models of phase transformation for Fe are illustrated in Fig. S12 (c). The morphology of irregular shape FeO(OH) nanoparticles synthesized by LPDD is depicted in the high magnification SEM and low magnification TEM images shown in Fig. S13 (a) and (b). Fig. S13 (c) displays an HR TEM image of a single nanoparticle, and its corresponding FFT pattern reveals a base centered monoclinic crystal structure imaged at a zone axis [2 1 3]. In comparison, Fig. S13 (d) and (e) show the low magnification SEM and TEM images of nanowire Fe after phase transformation. The HR TEM image taken from a nanowire indicates an FCC structure, as demonstrated by the index of the reciprocal image (inset in Fig. S13 (f)). The CVs comparison for FeO(OH) and Fe/carbon cloth electrodes were performed and shown in Fig. S13 (g-i).

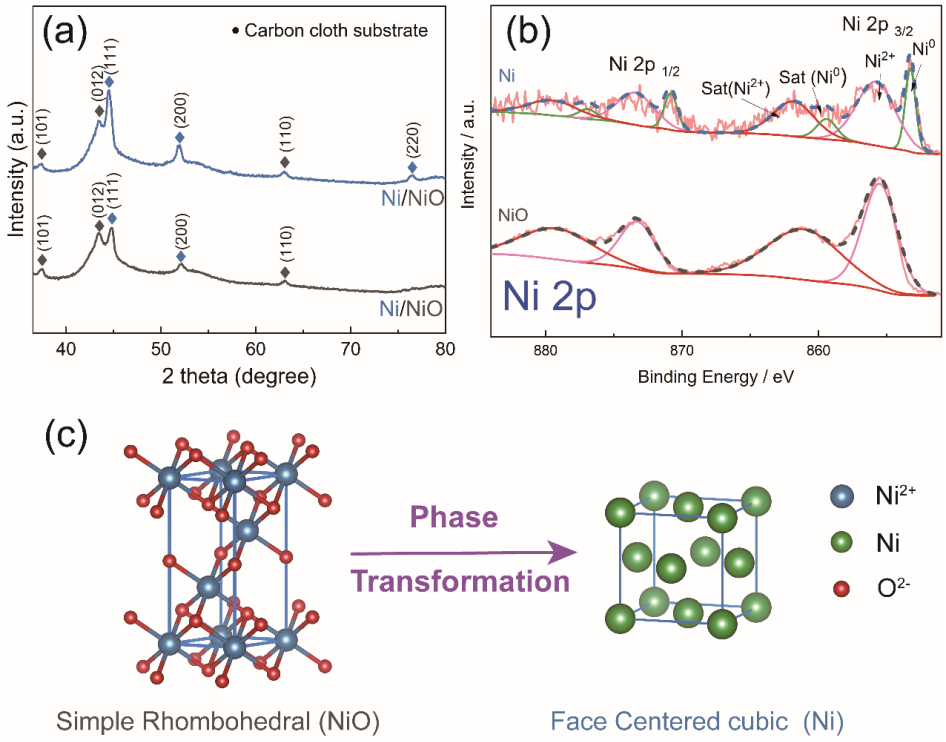

Fig. S14. (a) XRD and (b) XPS analysis of LPDD pre-synthesized NiO and laser irradiation phase transformed Ni/carbon cloth composites, (c) crystal structure models of NiO and Ni.

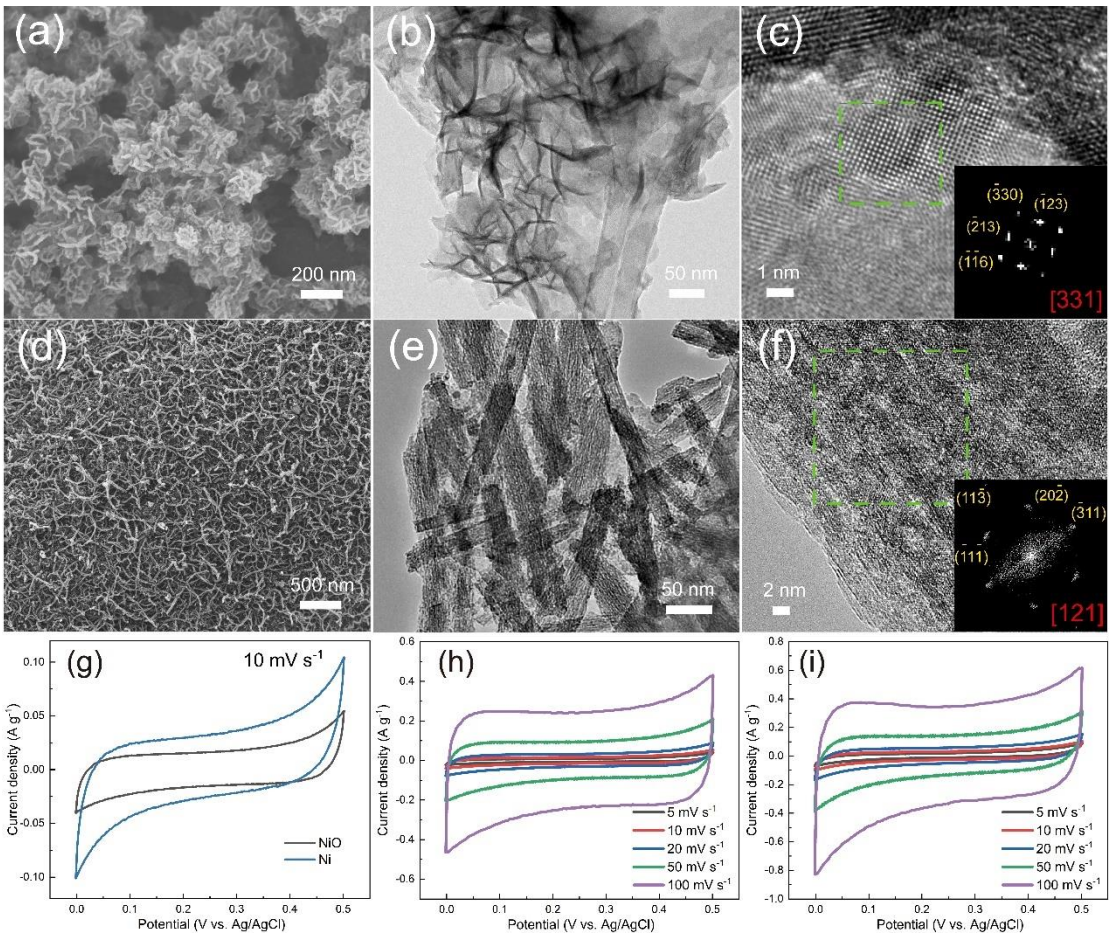

Fig. S15. (a) SEM, and (b) TEM images of LPDD synthesized NiO, (c) HR TEM image and its corresponding FFT pattern of NiO nanosheet; (d) SEM, and (e) TEM images of laser irradiation phase transformed Ni, (c) HR TEM image and its corresponding FFT pattern of Ni nanowire; (h) CV curves of NiO and Ni/carbon cloth electrodes at a scan rate of 10 mV s^{-1} in 1M Na_2SO_4 electrolyte, CV profiles of (i) NiO and (j) Ni/carbon cloth electrodes at different scan rates.

The XRD patterns of both LPDD pre-synthesized and phase transformed nickel oxide/carbon cloth electrodes are shown in Fig. S14 (a). The pre-synthesized sample shows the peaks at 37.5°, 43.5°, and 63.1°, attributing to (1 0 1), (0 1 2), and (1 1 0) planes of simple rhombohedral NiO crystal (JCPDS 78-7533), and the other two peaks at 44.8°, and 52.1° attributes to (1 1 1) and (2 0 0) planes of FCC Ni crystal (JCPDS 07-0510). Apart from the commonly shared peaks, the sample after laser irradiation exhibits an extra peak at 76.4°, attributed to the presence of FCC Ni crystal. In contrast, the XRD patterns of the sample without ethylene glycol during laser irradiation are displayed in Fig. S5 (e). Fig. S14 (c) presents the XPS HR spectra of the Ni 2p region for both samples. The deconvolution of the Ni 2p spectrum for both samples shows the common peaks at a binding energy of 873.5 eV, 855.79 eV corresponding to $Ni^{2+}2p_{1/2}$ and $Ni^{2+}2p_{3/2}$, and other two peaks attributing to sat (Ni^{2+}) peaks. In contrast, the deconvolution of phase transformed sample Ni 2 shows the additional peaks at 853.26, and 870.8 eV attributing to $Ni^{0}2p_{1/2}$ and $Ni^{0}2p_{3/2}$, and the peaks at 859.4 eV and 876.7 eV contributing to satellite peaks (Ni^{0}), consistent with reported data in the literature [11]. These XPS results demonstrate the phase transformation from NiO to Ni during laser irradiation. The crystal structure models

of phase transformation for nickel are illustrated in Fig. S14 (c). The high magnification SEM and low TEM images of the LPDD pre-synthesized nanosheet shape Ni/NiO mixture on carbon cloth substrate is shown in Fig. S15 (a) and (b). Fig. S15 (c) presents the HR TEM image of a single nanosheet and its corresponding FFT pattern, which reveals the simple rhombohedral lattice structure of NiO imaged at a zone axis [3 3 1]. While, the morphology of the nanosheet has been transformed to the nanowire on carbon cloth substrate after phase transformation via laser irradiation, as observed in the low magnification SEM and TEM images in Fig. S15 (d) and (e). The HR TEM image of a single nanowire was taken at a zone axis of [1 2 1], which matched the FCC crystal structure of Ni, and its corresponding FFT pattern is shown as an inset. The CVs comparison for NiO and Ni/carbon cloth electrodes were performed and shown in Fig. S15 (g-i).

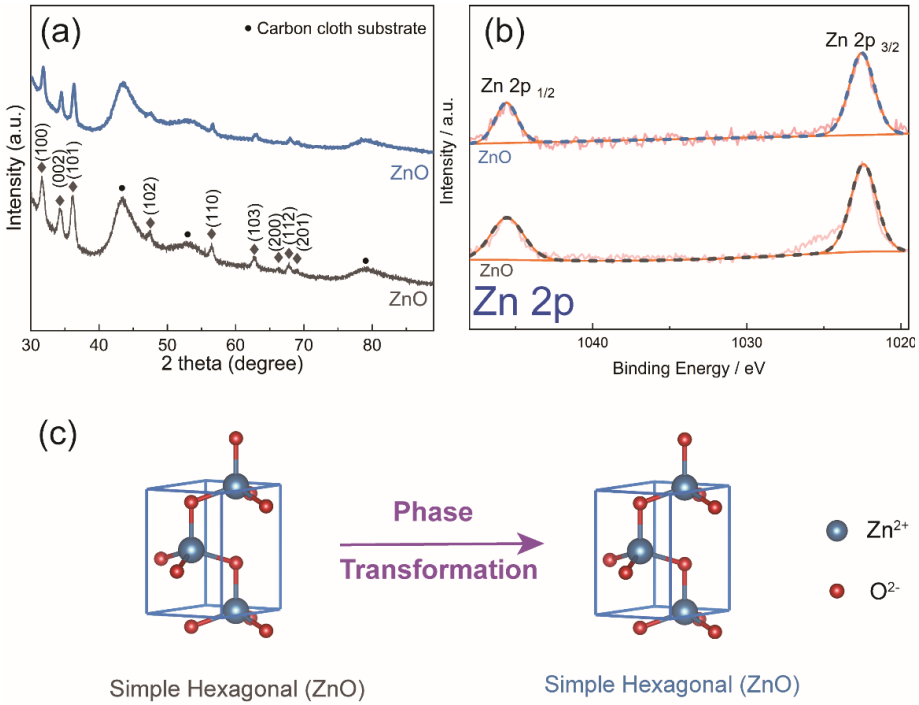

Fig. S16. (a) XRD and (b) XPS analysis of LPDD pre-synthesized and laser irradiation phase

transformed ZnO/carbon cloth composites, (c) crystal structure model of ZnO.

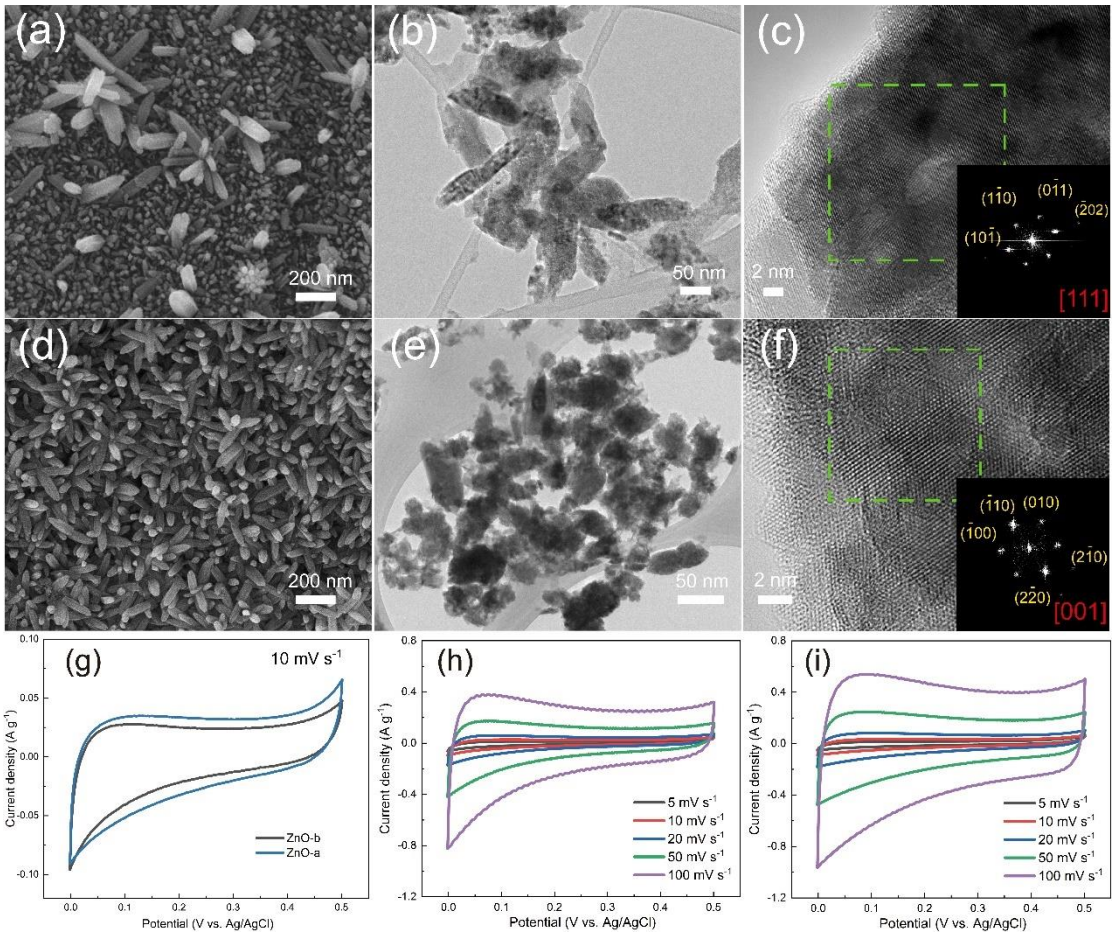

Fig. S17. (a) SEM, and (b) TEM images of LPDD synthesized ZnO, (c) HR TEM image and its corresponding FFT pattern of ZnO nanorice; (d) SEM, and (e) TEM images of laser irradiation phase transformed ZnO, (c) HR TEM image and its corresponding FFT pattern; (h) CV curves of both electrodes at a scan rate of 10 mV s^{-1} in 1M Na_2SO_4 electrolyte, (h) and (i) CV profiles of both electrodes at different scan rates.

Fig. S16 (a) presents the XRD pattern of LPDD pre-synthesized and phase transformed ZnO on the carbon cloth substrate. Both samples share the common peaks at 31.6°, 34.3°, 36.2°, 47.7°, 56.5°, 62.7°, 66.2°, 67.7°, and 69.2°, ascribed to (1 0 0), (0 0 2), (1 0 1), (1 0 2), (1 1 0), (1 0 3), (2 0 0), (1 1 2), and (2 0 1), respectively. These peaks indicate that the crystal structure of simple hexagonal ZnO (JCPDS 08-8199) remains unchanged upon laser irradiation. For comparison, the XRD

patterns for pre-synthesized, laser irradiation with and without ethylene glycol ZnO/carbon cloth electrode are displayed in Fig. S5 (f). Fig. S16 (b) displays the XPS HR spectra for the Zn 2p region of both samples, which show the same peaks at a binding energy of 1022.5 eV and 1042.6 eV attributed to $Zn^{2+}2p_{3/2}$ and $Zn^{2+}2p_{1/2}$. These peaks are consistent with reported data for ZnO [12] and demonstrate that no crystal structure changes during the laser irradiation process. The crystal structure models of ZnO are shown in Fig. S16 (c). High magnification SEM and low TEM images in Fig. S17 (a), (b), (d), and (e) show the morphologies of LPDD pre-synthesized and phase transformed ZnO. Both samples exhibit a nano rice shape with dimensions ranging from 50nm to 150 nm in length. The FFT pattern in the HR TEM image confirms the simple hexagonal crystal structure imaged at a zone axis [1 1 1] and [0 0 1] for pre-synthesized and phase transformed ZnO. This result provides evidence that no crystal structure changes occur during laser irradiation. The CVs for both samples were performed and shown in Fig. S17 (h-j).

References

[1] Minus M, Kumar S. *Jom*, 2005, 57: 52-58

[2] Jie C, Xiang X, Peng X. *Materials & Design*, 2009, 30: 1413-1416

[3] Nakouzi S, Pancrace J, Schmidt F M, Maoult Y L, Berthet F. *AIP Conference Proceedings, American Institute of Physics*, 2011, 1125-1130.

[4] Wallace W. *NIST standard reference database*, *Mass spectra*, 2018, 20899

[5] lstrup I, Chorkendorff I, Candia R, Clausen B S, Topsøe H. *Journal of Catalysis*, 1982, 77: 397-409

[6] Hedman J, Klasson M, Nilsson R, Nordling C, Sorokina M, Kljushnikov O, Nemnonov S, Trapeznikov V, Zyryanov V. *Physica Scripta*, 1971, 4: 195

[7] Agostinelli E, Battistoni C, Fiorani D, Mattogno G, Nogues M. *Journal of Physics and Chemistry of Solids*, 1989, 50: 269-272.

[8] Allen G C, Curtis M T, Hooper, A J, Tucker P M. *Journal of the Chemical Society, Dalton Transactions*, 1973, 1675-1683

[9] Tan B J, Klabunde K J, Sherwood P M. *Chemistry of Material*, 1990, 2: 186-191

[10] Mathieu H, Landolt D. *Corrosion science*, 1986, 26: 547-559

[11] Paparazzo E, Severini E, Jimenez-Lopez A, Maireles-Torres P, Olivera-Pastor P, Rodriguez-Castellon E, Tomlinson A A. *Journal of Materials Chemistry*, 1992, 2: 1175-1178

[12] Gaarenstroom S, Winograd N. *The Journal of Chemical Physics*, 1977, 67: 3500-3506